Phase-field crystal modeling and classical density functional theory of freezing

K. R. Elder,[1] Nikolas Provatas,[2] Joel Berry,[1,3] Peter Stefanovic,[2] and Martin Grant[3]
[1]*Department of Physics, Oakland University, Rochester, Michigan 48309-4487, USA*
[2]*Department of Materials Science and Engineering and Brockhouse Institute for Materials Research, McMaster University, Hamilton, Ontario, Canada L8S-4L7*
[3]*Physics Department, McGill University, 3600 rue University, Rutherford Building, Montréal, Québec, Canada H3A 2T8*
(Received 7 July 2006; revised manuscript received 25 November 2006; published 14 February 2007)

In this paper the relationship between the classical density functional theory of freezing and phase-field modeling is examined. More specifically a connection is made between the correlation functions that enter density functional theory and the free energy functionals used in *phase-field crystal* modeling and standard models of binary alloys (i.e., regular solution model). To demonstrate the properties of the phase-field crystal formalism a simple model of binary alloy crystallization is derived and shown to simultaneously model solidification, phase segregation, grain growth, elastic and plastic deformations in anisotropic systems with multiple crystal orientations on diffusive time scales.

DOI: 10.1103/PhysRevB.75.064107 PACS number(s): 64.60.My, 05.70.Ln, 64.60.Cn, 81.30.Hd

I. INTRODUCTION

The formalism for calculating equilibrium states was established many years ago by Gibbs, Boltzmann, and others. While this formalism has proved remarkably successful there are many systems which never reach equilibrium, mainly due to the existence of metastable or long-lived transient states. This is most apparent in solid materials. For example, it is very unlikely that the reader is sitting in a room containing any single crystals except items produced with considerable effort such as the silicon chips in computers. In fact the vast majority of naturally occurring or engineered materials are not in equilibrium and contain complex spatial structures on nanometer, micron or millimeter length scales. More importantly many material properties (electrical, optical, mechanical, etc.) are strongly influenced by the nonequilibrium structures that form during material processing. For example, the yield strength of a polycrystal varies as the inverse square of the average grain size.

The study of nonequilibrium microstructure formation has seen considerable advances through the use of the *phase-field* approach. This methodology models the dynamics of various continuum fields that collectively characterize microstructure in phase transformations. For example, phase-field or continuum models have been used to simulate spinodal decomposition,[1] order-disorder transition kinetics,[2] ordering of block-copolymer melts,[3] solidification of pure and binary systems[4–8] and many other systems. In these phenomena the evolution of the appropriate field(s) (e.g., solute concentration in spinodal decomposition) is assumed to be dissipative and driven by minimizing a phenomenological free energy functional.[1]

Advances in the phase-field modeling of solidification phenomena have followed a progression of innovations, beginning with the development of free energies that capture the thermodynamics of pure materials[4–6] and alloys.[7,8] Several modifications were then proposed[9–11] to simplify numerical simulations and improve computational efficiency. Perhaps the most important innovation was the development of matched asymptotic analysis techniques that directly connect phase-field model parameters with the classical Stefan (or sharp-interface) models for pure materials or alloys.[12–15] These techniques were complimented by new adaptive mesh refinement algorithms,[16,17] whose improved efficiency significantly increased the length scales accessible by numerical simulations, thus enabling the first experimentally relevant simulations of complex dendritic structures and their interactions in organic and metallic alloys.[18–22]

A weakness of the traditional phase-field methodology is that it is usually formulated in terms of fields that are spatially uniform in equilibrium. This eliminates many physical features that arise due to the periodic nature of crystalline phases, including elastic and plastic deformation, anisotropy and multiple orientations. To circumvent this problem traditional phase-field models have been augmented by the addition of one or more auxiliary fields used to describe the density of dislocations[23–25] continuum stress and strain fields[26,27] and orientation fields.[28–30] These approaches have proven quite useful in various applications such as polycrystalline solidification.[24,28–32] Nevertheless it has proven quite challenging to incorporate elastoplasticity, diffusive phase transformation kinetics and anisotropic surface energy effects into a single, thermodynamically consistent model.

Very recently a new extension to phase-field modeling has emerged known as the *phase-field crystal* method (PFC).[33–35] This methodology describes the evolution of the atomic density of a system according to dissipative dynamics driven by free energy minimization. In the PFC approach the free energy functional of a solid phase is minimized when the density field is periodic. As discussed in the literature[33–35] the periodic nature of the density field naturally gives rise to elastic effects, multiple crystal orientations and the nucleation and motion of dislocations. While these physical features are included in other atomistic approaches (such as molecular dynamics) a significant advantage of the PFC method is that, by construction, it is restricted to operate on diffusive time scales not on the prohibitively small time scales associated with atomic lattice vibrations. The approach is similar to the atomic density function theory that was recently proposed by Jin and Khachaturyan.[36] In the case of pure materials the PFC approach has been shown[33,34] to model many

phenomena dominated by atomic scale elastic and plastic deformation effects. These include grain boundary interactions, epitaxial growth, and the yield strength of nanocrystals.

The original PFC model is among the simplest mathematical descriptions that can selfconsistently combine the physics of atomic-scale elastoplasticity with the diffusive dynamics of phase transformations and microstructure formation. Nevertheless, analogously to traditional phase-field modeling of solidification, further work is required to fully exploit the methodology. More specifically it is important to be able to generalize the method to more complex situations (binary alloys, faster dynamics, different crystal structures, etc.), to develop more efficient numerical techniques and to make a direct connection of the parameters of the model to experimental systems. Several innovations toward this goal have already been developed. Goldenfeld *et al.*[37,38] have recently derived amplitude equations for the PFC model which are amenable to adaptive mesh refinement schemes. This work has the potential to enable simulations of mesoscopic phenomena ($\mu m \rightarrow mm$) that are resolved down to the atomic scale and incorporate all the physics discussed above. Another recent advance is the inclusion of higher order time derivatives in the dynamics to simulate "instantaneous" elastic relaxation.[39] This extension is important for modeling complex stress propagation and externally imposed strains. Very recently, Wu *et al.*[40,41] fitted the PFC parameters to experimental data in iron and were able to show that the PFC model gives an accurate description of the anisotropy of the surface tension. In addition to this work Wu and Karma have also developed a simple and elegant scheme to extend the method to other crystal symmetries (i.e., FCC in three dimensions).

The purpose of this paper is to link the formalism of classical density functional theory (DFT) of freezing, as formulated by Ramakrishnan and Yussouff[42] (and also reviewed by many other authors, such as Singh[43]) with the PFC method and to exploit this connection to develop a PFC model for binary alloys. The organization of the paper and a summary of the remaining sections is as follows.

In Sec. II A the classical density functional theory of freezing of pure and binary systems is briefly outlined. In this approach the free energy functional is written in terms of the time averaged atomic density field ρ (ρ_A and ρ_B in binary systems) and expanded around a liquid reference state existing along the liquid-solid coexistence line. Formally the expansion contains the n-point correlation functions of the liquid state. In this work the series expansion of the free energy is truncated at the two-point correlation function, $C(\vec{r}_1,\vec{r}_2)$.

Within this framework it is shown in Sec. III A that the PFC model for a pure material can be recovered from DFT if $C(\vec{r}_1,\vec{r}_2)$ is parametrized by three constants related to the liquid and solid state compressibilities and the lattice constant. The parameters of the PFC model can thus be directly related to the physical constants that enter the DFT of freezing and the PFC model can be viewed as a simplified form of DFT. In Sec. III B a binary system is considered. Similar to the case of pure materials the free energy expansion of a binary alloy will be truncated at the two-point correlation functions which are then characterized by three parameters. At this level of simplification it is shown that the "regular" solution model used in materials physics for alloys can be obtained directly from DFT. It is shown that the phenomenological nearest-neighbor bond energies that enter the "regular" solution model are equal to the compressibilities that enter DFT. This section also provides insight into the concentration dependence of various properties of the crystalline phase of a binary alloy such as the lattice constant, effective mobilities and elastic constants.

In Sec. III C a simplified version of the binary alloy free energy is derived. This is done in order to provide a mathematically simpler model that can more transparently illustrate the use of the PFC formalism in simultaneously modeling diverse processes such as solidification, grain growth, defect nucleation, phase segregation and elastic and plastic deformation. This section also shows that the free energy of the simplified alloy PFC model reproduces two common phase diagrams associated with typical binary alloys in materials science. Some of the more tedious calculations in the derivation of the simplified model are shown in the Appendix.

In Sec. IV dynamical equations of motion that govern the evolution of the solute concentration and density field of a binary alloy are derived. Finally in Sec. V the simplified binary alloy model is used to simulate several important applications involving the interplay of phase transformation kinetics and elastic and plastic effects. This includes solidification, epitaxial growth, and spinodal decomposition.

II. CLASSICAL DENSITY FUNCTIONAL THEORY OF FREEZING

In this section free energy functionals of pure and binary systems as derived from the classical density functional theory of freezing are presented. For a rigorous treatment of their derivation the reader is referred to the work of Ramakrishnan and Yussouff[42] and numerous other very closely related review articles by Singh,[43] Evans,[44] and references therein.

In DFT the emergence of an ordered phase during solidification can be viewed as a transition to a phase in which the atomic number density, $\rho(\vec{r})$, is highly nonhomogenous and possesses the spatial symmetries of the crystal.[43] This approach implicitly integrates out phonon modes in favor of a statistical view of the ordered phase that changes on diffusive time scales. The free energy functional of a system is expressed in terms of ρ and constitutes the starting point of the PFC model.

In this work the free energy functional, denoted $\mathcal{F}[\rho]$, is expanded functionally about a density, $\rho=\rho_l$, corresponding to a liquid state lying on the liquidus line of the solid-liquid coexistence phase diagram of a pure material as shown in Fig. 1(a). The expansion is performed in powers of $\delta\rho \equiv \rho - \rho_l$.

As shown by others[42–44] the free energy density can be written as

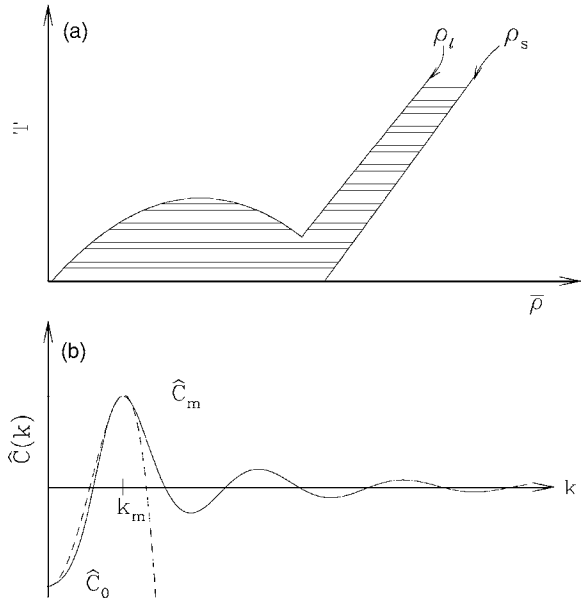

FIG. 1. (a) Sample phase diagram. In this figure the shaded area corresponds to a coexistence region. In the calculations presented in this paper the correlation functions are taken from points along the liquidus line at density ρ^{ℓ}. (b) In this figure a typical liquid state two-point direct correlation function is sketched. The dashed line represents the approximation used in most of the paper.

$$\mathcal{F}_c/k_BT = \int d\vec{x}\{\rho(\vec{r})\ln[\rho(\vec{r})/\rho_l] - \delta\rho(\vec{r})\} - \sum_{n=2}^{\infty}\frac{1}{n!}\int\prod_{i=1}^{n} d\vec{r}_i\delta\rho(\vec{r}_i)C_n(\vec{r}_1,\vec{r}_2,\vec{r}_3,\ldots,\vec{r}_n), \quad (1)$$

where $\mathcal{F}_c$ is the free energy corresponding to the density $\rho(\vec{r})$ minus that at the constant density ρ_l, and the C_n functions are n-point direct correlation functions of an isotropic fluid. Formally the correlation functions are defined by

$$C_n(\vec{r}_1,\vec{r}_2,\vec{r}_3,\ldots) \equiv \frac{\delta^n\Phi}{\prod_{i=n}\delta\rho(\vec{r}_i)}, \quad (2)$$

where $\Phi[\rho]$ represents the total potential energy of interactions between the particles in the material. A particularly simple proof that Φ is a functional of ρ is given in Evans.[44]

For an alloy involving one or more components the free energy functional of a pure material in Eq. (1) is extended to the form

$$\frac{\mathcal{F}_c}{k_BT} = \sum_i \int d\vec{r}\{\rho_i(\vec{r})\ln[\rho_i(\vec{r})/\rho_\ell^i] - \delta\rho_i(\vec{r})\} - \frac{1}{2}\sum_{i,j}\int d\vec{r}_1 d\vec{r}_2\delta\rho_i(\vec{r}_1)C^{ij}\delta\rho_j(\vec{r}_2) + \cdots, \quad (3)$$

where the sums are over the elements in the alloy, $\delta\rho_i \equiv \rho_i - \rho_\ell^i$ and ρ_ℓ^i is the value of the number density of component i on the liquid-side of the liquid-solid coexistence line. The function C^{ij} is the two-point direct correlation function of between components i and j in an isotropic fluid. As in the case of pure materials it will be assumed that $C^{ij} \equiv C^{ij}(|\vec{r}_1 - \vec{r}_2|)$. The next term in the expansion of Eq. (3) contains the three-point correlation, the next after that, the four point, etc. In this paper only two-point correlations will be considered, but it must be stressed that these higher order correlations may be crucial for some systems, such as Si. Before considering the properties of the binary alloy free energy in detail it is instructive to first study the properties of a pure system and show the connection between this formalism and the original PFC model.

III. ANALYSIS OF FREE ENERGY FUNCTIONALS

A. Pure materials

In this section the free energy functional of a single component alloy is considered in the limit that the series given in Eq. (1) can be truncated at C_2, i.e.,

$$\mathcal{F}/k_BT = \int d\vec{r}[\rho\ln(\rho/\rho_\ell) - \delta\rho] - (1/2)\int d\vec{r}d\vec{r}\delta\rho C(\vec{r},\vec{r})\delta\rho' \quad (4)$$

where, for convenience, the subscript 2 has been dropped from the two-point correlation function as has the subscript c from $\mathcal{F}_c$. To understand the basic features of this free energy functional it is useful to expand $\mathcal{F}$ in the dimensionless deviation of the density ρ from its average, $\bar{\rho}$, using the rescaled density

$$n \equiv (\rho - \bar{\rho})/\bar{\rho}. \quad (5)$$

Expanding $\mathcal{F}$ in powers of n gives

$$\frac{\Delta\mathcal{F}}{\bar{\rho}k_BT} = \int d\vec{r}\left(n\frac{1-\bar{\rho}C}{2}n - \frac{n^3}{6} + \frac{n^4}{12} - \cdots\right), \quad (6)$$

where $\Delta\mathcal{F} \equiv \mathcal{F} - \mathcal{F}_0$ and $\mathcal{F}_0$ is the the free energy functional at constant density (i.e., $\rho = \bar{\rho}$). For simplicity C is an operator defined such that $nCn \equiv \int d\vec{r}'n(\vec{r})C(|\vec{r}-\vec{r}'|)n(\vec{r}')$. Terms that are linearly proportional to n in the above integral are identically zero by definition.

To gain insight into the properties of the free energy functional in Eq. (6) it is useful to expand the two-point correlation function in a Taylor series around $k=0$, i.e.,

$$\hat{C} = \hat{C}_0 + \hat{C}_2k^2 + \hat{C}_4k^4 + \cdots. \quad (7)$$

[in real space this corresponds to $C = (\hat{C}_0 - \hat{C}_2\nabla^2 + \hat{C}_4\nabla^4 - \cdots)\delta(\vec{r}-\vec{r}')$, where the gradients are with respect to $\vec{r}'$]. The function $\hat{C}$ is sketched for a typical liquid in Fig. 1(b). In what follows only terms up to k^4 will be retained. In this manner the properties of the material are parametrized by the three variables, $\hat{C}_0$, $\hat{C}_2$, and $\hat{C}_4$. To fit the first peak in $\hat{C}$, $\hat{C}_0$, $\hat{C}_2$, and $\hat{C}_4$ must be negative, positive, and negative, respectively. These variables are related to three basic properties of the material, the liquid phase isothermal compressibility

$[\sim(1-\bar{\rho}\hat{C}_0)]$, the bulk modulus of the crystal $(\sim\bar{\rho}\hat{C}_2^2/|\hat{C}_4|)$ and lattice constant $[\sim(\hat{C}_2/|\hat{C}_4|)^{1/2}]$. In other words the $k=0$ term is related to the liquid phase isothermal compressibility, the height of the first peak [$\hat{C}_m$ in Fig. 1(b)] is related to the bulk modulus of the crystalline phase and the position of the first peak determines the lattice constant.

It is important to note that at this level of simplification the material is only defined by three quantities which may not be enough to fully parametrize any given material. For example, this simple three parameter model always predicts triangular symmetry in two dimensions and BCC symmetry in three dimensions. Other crystal symmetries can be obtained by using more complicated two-point correlation functions[40,41] or by including higher order correlation functions. In addition it is possible that fitting to the width, height, and position of the first peak in $\hat{C}$ may lead to a more accurate fitting to experimental data.

In two dimensions $\mathcal{F}$ is minimized by a triangular lattice that can be represented to lowest order by a one-mode approximation as

$$n = A\left[\frac{1}{2}\cos\left(\frac{2qy}{\sqrt{3}}\right) - \cos(qx)\cos\left(\frac{qy}{\sqrt{(3)}}\right)\right]. \tag{8}$$

Substituting Eq. (8) into Eq. (6) and minimizing with respect to q gives equilibrium wave vector of

$$q_{\mathrm{eq}} = \sqrt{3\hat{C}_2/(8|\hat{C}_4|)} \tag{9}$$

or in terms of the equilibrium lattice constant $a_{\mathrm{eq}}=2\pi/q_{\mathrm{eq}}$. When $q=q_{\mathrm{eq}}$, $\Delta\mathcal{F}$ becomes

$$\Delta F = \tfrac{3}{16}\Delta B A^2 - \tfrac{1}{32}A^3 + \tfrac{15}{512}A^4 + \cdots, \tag{10}$$

where $\Delta F \equiv \Delta\mathcal{F}/(\bar{\rho}k_BTS)$, S is the area of a unit cell, $\Delta B \equiv B^\ell - B^s$, $B^\ell \equiv 1-\bar{\rho}\hat{C}_0$, and $B^s \equiv \bar{\rho}(\hat{C}_2)^2/(4|\hat{C}_4|)$. The parameter B^ℓ is the dimensionless bulk modulus of the liquid state [i.e., $B^\ell=\kappa/(\bar{\rho}k_BT)$, where κ is the bulk modulus of a liquid]. The parameter B_s is proportional to the bulk modulus in the crystalline phase.

Equation (10) indicates that the liquid state is linearly unstable to the formation of the crystalline phase when $\Delta B<0$. This instability arises from a competition between the elastic energy stored in the liquid and crystalline phases. It is interesting to note that ΔB can also be written

$$\Delta B = (\bar{\rho}_s - \bar{\rho})/\bar{\rho}_s, \tag{11}$$

where $\bar{\rho}_s = 1/\hat{C}_m$ and $\hat{C}_m$ is the height of the first peak of $\hat{C}$ as shown in Fig. 1. Written in this form $\bar{\rho}_s$ can be thought of as defining the effective spinodal density, i.e., the average density at which the liquid becomes linearly unstable to crystallization.

Unfortunately it is difficult to obtain the equilibrium state (i.e., by solving $d\Delta F/dA=0$) without truncating the infinite series in Eq. (10). If only terms to order A^4 are retained an analytic approximation can be obtained for the amplitude (A_{min}) that minimizes $\mathcal{F}$. In this approximation the solution is $A_{\mathrm{min}}=2(1+\sqrt{20\bar{\rho}/\bar{\rho}_s-19})/5$. Thus solutions for a crystalline state exist when $\bar{\rho}>19/20\bar{\rho}_s$.

It is also straightforward to calculate the change in energy of the crystalline state upon deformation (i.e., bulk, shear or deviatoric). Details of similar calculations are given in the literature.[33,34] The result of these two-dimensional calculations gives the dimensionless bulk modulus, B_c, of the crystalline phase, i.e.,

$$B_c = \frac{3}{32}\bar{\rho}\frac{(\hat{C}_2)^2}{|\hat{C}_4|}A_{\mathrm{min}}^2 = \frac{3}{8}B^sA_{\mathrm{min}}^2. \tag{12}$$

In other words the parameter B^s controls the bulk modulus of the crystalline phase.

These calculations can be easily extended to three dimensions. As discussed previously this particular approximation for $\hat{C}$ leads to a BCC crystal in three dimensions which can be represented in a one mode approximation as, $n=A[\cos(qx)\cos(qy)+\cos(qx)\cos(qz)+\cos(qy)\cos(qz)]$. Substituting this functional form into the free energy and minimizing with respect to q gives, $q_{\mathrm{eq}}^{3d}=\sqrt{\hat{C}_2/|\hat{C}_4|}$, and the free energy functional at this q is

$$\Delta F^{3d} = \tfrac{3}{8}\Delta B A^2 - \tfrac{1}{8}A^3 + \tfrac{45}{256}A^4 + \cdots. \tag{13}$$

Thus in this instance the spinodal occurs at the same density as in the two-dimensional case. If the series is truncated at A^4 the amplitude that minimizes the free energy is then $A_{\mathrm{min}}^{3d}=4(1+\sqrt{15\bar{\rho}/\bar{\rho}_s-14})/15$. Thus in this approximations crystalline (BCC) solutions only exist if $\bar{\rho}>14\bar{\rho}_s/15$. In addition the elastic constants can also be calculated in three-dimensions (3D) in the usual manner. For example, the dimensionless bulk modulus of the crystalline state is given by $B_c^{3d}=3B^s(A_{\mathrm{min}}^{3d})^2$. This calculation gives the basic functional dependence of the (dimensionless) bulk modulus on B^s and the amplitude. For a more accurate calculation higher order Fourier components and more terms in the powers series in n should be retained.

Finally it is useful to consider fixing the density and varying the temperature. If the liquidus and solidus lines are roughly linear then, $\bar{\rho}_s$ can be approximated by a linear function of temperature. In the sample phase diagram shown in Fig. 1(a) the liquidus and solidus lines are roughly parallel and it is likely that the spinodal is also roughly parallel to these lines. In this case ΔB can be written

$$\Delta B = \alpha\Delta T, \tag{14}$$

where $\Delta T \equiv (T-T_s)/T_s$, T_s is the spinodal temperature and $\alpha \equiv (T_s/\bar{\rho}_s)(\partial\bar{\rho}_s/\partial T_s)$, evaluated at $\rho=\bar{\rho}$.

B. Binary alloys

For a binary alloy made up of A and B atoms the free energy functional can be written to lowest order in terms of the direct correlation functions as

$$\frac{\mathcal{F}}{k_BT} = \int d\vec{r}\left[\rho_A \ln\left(\frac{\rho_A}{\rho_\ell^A}\right) - \delta\rho_A + \rho_B \ln\left(\frac{\rho_B}{\rho_\ell^B}\right) - \delta\rho_B\right] - \frac{1}{2}\int d\vec{r}_1 d\vec{r}_2 [\delta\rho_A(\vec{r}_1)C^{AA}(\vec{r}_1,\vec{r}_2)\delta\rho_A(\vec{r}_2) + \delta\rho_B(\vec{r}_1)C^{BB}(\vec{r}_1,\vec{r}_2)\delta\rho_B(\vec{r}_2) + 2\delta\rho_A(\vec{r}_1)C^{AB}(\vec{r}_1,\vec{r}_2)\delta\rho_B(\vec{r}_2)], \quad (15)$$

where $\delta\rho_A \equiv \rho_A - \rho_l^A$ and $\delta\rho_B \equiv \rho_B - \rho_l^B$. It is assumed here that all two-point correlation functions are isotropic, i.e., $C^{ij}(\vec{r}_1,\vec{r}_2) = C^{ij}(|\vec{r}_1 - \vec{r}_2|)$.

In order to make a connection between the alloy free energy and standard phase-field models it is useful to define the total number density, $\rho \equiv \rho_A + \rho_B$ and a local concentration field $c \equiv \rho_A/\rho$. In terms of these fields the atomic densities can be written, $\rho_A = c\rho$ and $\rho_B = \rho(1-c)$. Furthermore it is useful to define $\rho = \rho_l + \delta\rho$ where $\rho_l \equiv \rho_l^A + \rho_l^B$ and $\delta c = 1/2 - c$. Substituting these definitions into Eq. (15) gives

$$\frac{\mathcal{F}}{k_BT} = \int d\vec{r}\left\{\rho \ln(\rho/\rho_\ell) - \delta\rho + \beta\delta c + F_0 - \frac{1}{2}\delta\rho[cC^{AA} + (1-c)C^{BB}]\delta\rho + \rho[c\ln(c) + (1-c)\ln(1-c)] + \rho c[(C^{AA} + C^{BB})/2 - C^{AB}](1-c)\rho\right\}, \quad (16)$$

where $\beta \equiv \rho_l(C^{AA} - C^{BB})(\rho + \rho_l)/2 + \rho \ln(\rho_\ell^B/\rho_\ell^A)$ and $F_0 \equiv \bar{\rho}\ln[\rho_\ell/(\rho_\ell^A\rho_\ell^B)^{1/2}] - C^{AA}/2[(\rho_\ell^A)^2 + \rho_l/2(\rho_l + \bar{\rho})] - C^{BB}/2[(\rho_\ell^B)^2 + \rho_l/2(\rho_l + \bar{\rho})]$.

To illustrate the properties of the model in Eq. (16) it useful to consider two limiting cases, a liquid phase at constant density and a crystalline phase at constant concentration. These calculations are presented in the following two sections.

1. Liquid phase properties

In the liquid phase ρ is constant on average and in the mean field limit can be replaced by $\rho = \bar{\rho}$. To simplify calculations, the case $\rho = \bar{\rho} \approx \rho_\ell$ (or $\delta\rho \approx 0$) will now be considered. As in the preceding section it is useful to expand the direct correlation functions in Fourier space, i.e.,

$$\hat{C}^{ij} = \hat{C}_0^{ij} + \hat{C}_2^{ij}k^2 + \hat{C}_4^{ij}k^4 + \cdots . \quad (17)$$

where the subscript i and j refer to a particular element. Substituting the real-space counterpart of the Fourier expansion for $\hat{C}^{ij}$ (to order k^2) into Eq. (16) gives

$$\frac{\mathcal{F}_C}{\bar{\rho}k_BT} = \int d\vec{r}\left(c\ln(c) + (1-c)\ln(1-c) + \frac{\bar{\rho}\Delta\hat{C}_0}{2}c(1-c) + \gamma^\ell\delta c + \frac{\bar{\rho}\Delta\hat{C}_2}{2}|\nabla c|^2\right), \quad (18)$$

where $\mathcal{F}_C$ is the total free energy minus a constant that depends only on $\bar{\rho}$, ρ_A^l, and ρ_B^l,

$$\gamma^\ell \equiv (B_\ell^{BB} - B_\ell^{AA}) + \bar{\rho}\ln(\rho_\ell^B/\rho_\ell^A), \quad (19)$$

$$\Delta\hat{C}_n \equiv \hat{C}_n^{AA} + \hat{C}_n^{BB} - 2\hat{C}_n^{AB}, \quad (20)$$

and $B_\ell^{ij} = 1 - \bar{\rho}\hat{C}_0^{ij}$ is the dimensionless bulk compressibility. Equation (18) is the regular solution model of a binary alloy in the limit $\gamma^\ell = 0$. It is also noteworthy that Eq. (18) implies a temperature dependence of the gradient energy coefficient which is consistent with other theoretical[65] and experimental[66] studies.

The coefficient of $c(1-c)$ in Eq. (18) is given by

$$\bar{\rho}\Delta\hat{C}_0 = 2B_\ell^{AB} - B_\ell^{AA} - B_\ell^{BB}. \quad (21)$$

This result shows that in the liquid state the interaction energies that enter regular solution free energies are simply the compressibilities (or the elastic energy) associated with the atomic species. The γ^ℓ term is also quite interesting as it is responsible for asymmetries in the phase diagram. Thus Eq. (19) implies that asymmetries can arise from either different compressibilities or different densities.

Expanding Eq. (18) around $c = 1/2$ gives

$$\frac{\Delta\mathcal{F}_C}{\bar{\rho}k_BT} = \int d\vec{r}\left(\frac{r^\ell}{2}\delta c^2 + \frac{u}{4}\delta c^4 + \gamma^\ell\delta c + \frac{K}{2}|\nabla c|^2\right), \quad (22)$$

where $\Delta\mathcal{F}_C \equiv \mathcal{F}_C - \bar{\rho}k_BT\int d\vec{r}[\bar{\rho}\Delta\hat{C}_0/8 - \ln(2)]$, $u \equiv 16/3$, $r^\ell \equiv (4 - \bar{\rho}\Delta\hat{C}_0)$, and $K = \bar{\rho}\Delta\hat{C}_2$. The parameter r^ℓ is related only to the $k = 0$ part of the two-point correlation function and can be written

$$r^\ell = 4 + (B_\ell^{AA} + B_\ell^{BB} - 2B_\ell^{AB}). \quad (23)$$

This result implies that the instability to phase segregation in the fluid is a competition between entropy (4) and the elastic energy of a mixed fluid ($2B_\ell^{AB}$) with the elastic energy associated with a phase separated fluid ($B_\ell^{AA} + B_\ell^{BB}$). Replacing the dimensionless bulk moduli with the dimensional version (i.e., $B = \kappa/k_BT$), gives the critical point (i.e., $r^l = 0$) as

$$T_C^\ell = (2\kappa_{AB} - \kappa_{BB} - \kappa_{AA})/(4k_B), \quad (24)$$

where κ is the dimensional bulk modulus.

The properties of the crystalline phase are more complicated but at the simplest level the only real difference is that the elastic energy associated with the crystalline state must be incorporated. This is discussed in the next section.

2. Crystalline phase properties

To illustrate the properties of the crystalline state, the case in which the concentration field is a constant is considered. In this limit the free energy functional given in Eq. (16) can be written in the form

$$\frac{\mathcal{F}}{k_BT} \equiv \int d\vec{r}\left[\rho\ln\left(\frac{\rho}{\rho_\ell}\right) - \delta\rho - \frac{1}{2}\delta\rho\bar{\bar{C}}\delta\rho + G\right], \quad (25)$$

where G is a function of the concentration c and ρ_l and couples only linearly to $\delta\rho$. The operator $\bar{\bar{C}}$ can be written as

$$\bar{\bar{C}} \equiv c^2C^{AA} + (1-c)^2C^{BB} + 2c(1-c)C^{AB}. \quad (26)$$

Thus in the limit that the concentration is constant this free energy functional is that of a pure material with an effective

two-point correlation function that is an average over the AA, BB, and AB interactions. In this limit the calculations presented in Sec. III A can be repeated using the same approximations (i.e., expanding ρ around ρ_ℓ, expanding $\bar{\bar{C}}$ to ∇^4 and using a one mode approximation for $\delta\rho$) to obtain predictions for the concentration dependence of various quantities. For example, the concentration dependence of the equilibrium wave vector [or lattice constant, Eq. (9)] and bulk modulus Eq. (12) can be obtained by redefining $\hat{C}_n = c^2\hat{C}_n^{AA} + (1-c)^2\hat{C}_n^{BB} + 2c(1-c)\hat{C}_n^{AB}$.

As a more specific example the equilibrium lattice constant can be expanded around $c=1/2$ to obtain in two or three dimensions,

$$a_{\mathrm{eq}}(\delta c) = a_{\mathrm{eq}}(0)(1 + \eta\delta c + \cdots), \tag{27}$$

where $\delta c = c - 1/2$ and η is the solute expansion coefficient given by

$$\eta = (\delta\hat{C}_4 - \delta\hat{C}_2)/2, \tag{28}$$

where

$$\delta\hat{C}_n \equiv (\hat{C}_n^{AA} - \hat{C}_n^{BB})/\hat{\bar{C}}_n \tag{29}$$

and $\hat{\bar{C}}_n \equiv \hat{C}_n(\delta c=0) = (\hat{C}_n^{AA} + \hat{C}_n^{BB} + 2\hat{C}_n^{AB})/4$.

This line of reasoning can also be used to understand the influence of alloy concentration on crystallization. Specifically, for the case of an alloy, the terms in Eq. (10) (with A replaced with A_{min}) become functions of concentration, since ΔB and A_{min} are concentration dependent. Here, ΔB can be expanded around $c=1/2$, i.e.,

$$\Delta B(\delta c) = \Delta B_0 + \Delta B_1\delta c + \Delta B_2\delta c^2 + \cdots, \tag{30}$$

where $\Delta B_0 = B_0^l - B_0^s$, $\Delta B_1 = B_1^l - B_1^s$, and $\Delta B_2 = B_2^l - B_2^s$ are determined in the Appendix. This would imply that in the crystalline phase the free energy has a term of the form, $r^c(\delta c)^2$, where

$$r^c = r^\ell + 3\Delta B_2 A_{\mathrm{min}}^2/8 \tag{31}$$

in two dimensions (in three dimensions the 3/8 factor is replaced with 3/4). This result indicates that crystallization (i.e., a nonzero A_{min}) favors phase segregation, assuming $\kappa_{AA} + \kappa_{BB} < 2\kappa_{AB}$. For example, when $B_2^s = 0$, the critical temperature increases and can be written

$$T_C^c = T_C^\ell(1 + 3A_{\mathrm{min}}^2/8), \tag{32}$$

or $T_C^c = T_C^\ell(1 + 3A_{\mathrm{min}}^2/4)$ in three dimensions.

C. Simple binary alloy model

In this section a simple binary alloy model is proposed based on a simplification of the free energy in Eq. (16). The goal of this section is to develop a mathematically *simple* model that can be used to simultaneously model grain growth, solidification, phase segregation in the presence of elastic and plastic deformation. To simplify calculations it is convenient to first introduce the following dimensionless fields:

$$n_A \equiv (\rho_A - \bar{\rho}_A)/\bar{\rho},$$

$$n_B \equiv (\rho_B - \bar{\rho}_B)/\bar{\rho}. \tag{33}$$

Also, it is convenient to expand in the following two fields:

$$n = n_A + n_B,$$

$$\delta N = (n_B - n_A) + \frac{\bar{\rho}_B - \bar{\rho}_A}{\bar{\rho}}. \tag{34}$$

The following calculations will use the field δN instead of δc. Expanding Eq. (16) around $\delta N=0$ and $n=0$ gives a free energy of the form

$$\frac{\mathcal{F}}{\bar{\rho}k_BT} = \int d\vec{r}\left(\frac{n}{2}[B^\ell + B^s(2R^2\nabla^2 + R^4\nabla^4)]n + \frac{t}{3}n^3 - \frac{v}{4}n^4 + \gamma\delta N + \frac{w}{2}\delta N^2 + \frac{u}{4}\delta N^4 + \frac{L^2}{2}|\vec{\nabla}\delta N|^2 + \cdots\right). \tag{35}$$

Details of this free energy and explicit expressions for B^ℓ, B^s, R, γ, w, and L are given in the Appendix. The variables t, v, and u are constants. For simplicity the calculations presented in this section are for a two-dimensional system.

The transition from liquid to solid is intimately related to $\Delta B = B^\ell - B^s$ as was the case for the pure material and can be written in terms of a temperature difference, i.e., Eq. (14). In addition some of the polynomial terms in n and δN have been multiplied by variable coefficients (t, v, and u) even though they can be derived exactly as shown in the Appendix. For example, the parameter $v=1/3$ recovers the exact form of the n^4 term. This flexibility in the choice of coefficients was done to be able to match the parameters of the free energy with experimental material parameters. As an example[40,41] showed that adjusting the parameter v can be used to match the amplitude of fluctuations obtained in molecular dynamics simulations. With this fit they are able to accurately predict the anisotropy of the surface energy of a liquid-crystal interface in iron.

To facilitate the calculation of the lowest order phase diagram corresponding to Eq. (35) it is convenient to assume the concentration field δN varies significantly over length scales much larger than the atomic number density field n. As a result, the density field can be integrated out of the free energy functional. Also, in the spirit of keeping calculations as simple as possible without losing the basic physics contained in the model, $\gamma=0$ in the free energy. In this instance the one-mode approximation for the total density, i.e., $n = A[\cos(2qy/\sqrt{3})/2 - \cos(qx)\cos(qy\sqrt{3})]$ will be used. Substituting this expression into Eq. (35) and minimizing with respect to q and A (recalling that δN is assumed constant over the scale that n varies) gives $q_{\mathrm{eq}} = \sqrt{3}/(2R)$ and $A_{\mathrm{min}} = 4(t + \sqrt{t^2 - 15v\Delta B})/15v$. The free energy that is minimized with respect to amplitude and lattice constant is then,

$$F_{\mathrm{sol}} = \frac{w}{2}\delta N^2 + \frac{u}{4}\delta N^4 + \frac{3}{16}\Delta B A_{\mathrm{min}}^2 - \frac{t}{16}A_{\mathrm{min}}^3 + \frac{45v}{512}A_{\mathrm{min}}^4. \tag{36}$$

For mathematical simplicity all further calculations will be limited to the approximations $B^{\ell}=B_0^{\ell}+B_2^{\ell}(\delta N)^2$ and $B^s=B_0^s$. In this limit analytic expressions can be obtained for a number of quantities and the free energy functional is still general enough to produce for example a eutectic phase diagram.

It is relatively simple to calculate the solid-solid coexistance curves by expanding $F_{\rm sol}$ to order $(\delta N)^4$, which then yields the solid-solid coexistence concentrations at low temperatures according to

$$\delta N_{\rm coex} = \pm\sqrt{|a|/b}, \tag{37}$$

where $a \equiv w+3B_2^{\ell}(A_{\rm min}^0)^2/8$, $b \equiv u-6(B_2^{\ell})^2 A_{\rm min}^0/(15vA_{\rm min}^0 - 4t)$ and $A_{\rm min}^0 \equiv A_{\rm min}(\delta N=0)$ (which is thus a function of ΔB_0). The critical temperature, ΔB_0^C is determined by setting $\delta N_{\rm coex}=0$ and solving for ΔB_0, which gives

$$\Delta B_0^c = (15wv - 2t\sqrt{-6B_2^{\ell}w})/(6B_2^{\ell}). \tag{38}$$

To obtain the liquid-solid coexistence lines the free energy of the liquid state must be compared to that of the solid. The mean field free energy of the liquid state is obtained by setting $n=0$ which gives

$$F_{\rm liq} = \frac{w}{2}\delta N^2 + \frac{u}{4}\delta N^4. \tag{39}$$

To obtain the solid-liquid coexistence lines it is useful to expand the free energy of the liquid and solid states around the value of δN at which the liquid and solid states have the same free energy, i.e., when $F_{\rm sol}=F_{\rm liq}$. This occurs when, $\delta N_{ls}=\pm\sqrt{(\Delta B_0^{ls}-\Delta B_0)/B_2^{\ell}}$, where $\Delta B_0 \equiv B_0^l - B_0^s$ and $\Delta B_0^{ls} \equiv 8t^2/(135v)$ is the lowest value of ΔB_0 at which a liquid can coexist with a solid. To complete the calculations, $F_{\rm sol}$ and $F_{\rm liq}$ are expanded around δN_{ls} to order $(\delta N-\delta N_{ls})^2$ and Maxwell's equal area construction rule can be used to identify the liquid-solid coexistence lines. The liquid-solidus lines are

$$\delta N_{\rm liq}/\delta N_{ls} = 1 + G(1-\sqrt{b_{\rm sol}/b_{\rm liq}}),$$

$$\delta N_{\rm sol}/\delta N_{ls} = 1 + G(1-\sqrt{b_{\rm liq}/b_{\rm sol}}), \tag{40}$$

where $G \equiv -8t^2/[135v(4\Delta B_0 - 3\Delta B_0^{ls})]$, $b_{\rm liq}=(w+3u\delta N_{ls}^2)/2$ and $b_{\rm sol}=b_{\rm liq}+2B_2^{\ell}(4\Delta B_0-3\Delta B_0^{ls})/(5v)$, for $\delta N_{\rm liq}>0$, $\delta N_{\rm sol}>0$ and similar results for $\delta N_{\rm liq}<0$, $\delta N_{\rm sol}<0$, since F is a function of δN^2 in this example. The calculations in this section and the preceding section are reasonably accurate when $\Delta B_0^{ls} > \Delta B_0^c$, however in the opposite limit a eutectic phase diagram forms and the accuracy of the calculations decreases. This case will be discussed below.

1. Linear elastic constants

As shown in previous literature,[33,34] the elastic constants can be calculated analytically in a one mode approximation by considering changes in F as a function of strain. For the binary model similar calculations can be made in a constant δN approximation and give

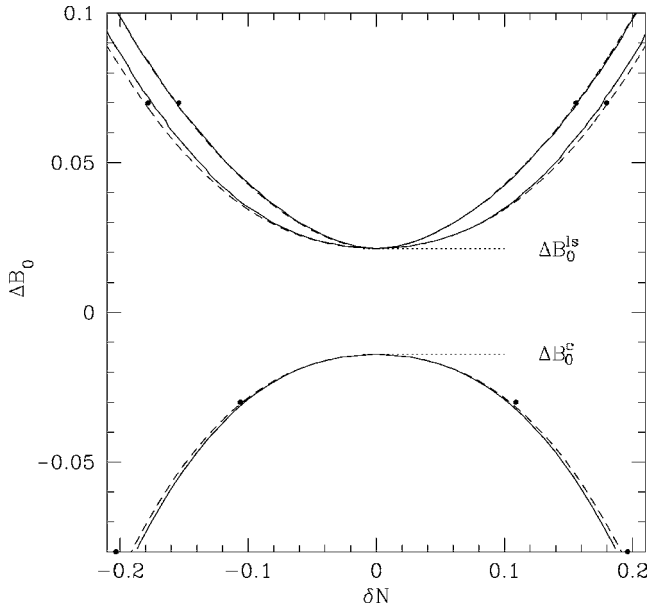

FIG. 2. Phase diagram of ΔB_0 vs δN for the parameters $B_0^s=1.00$, $B_1^{\ell}=0$, $B_2^{\ell}=-1.80$, $t=0.60$, $v=1.00$, $w=0.088$, $u=4.00$, $L=4.00$, $\gamma=0$, $R_0=1.00$, and $R_1=1.20$ [see Eq. (A4) for definitions of R_0 and R_1]. The solid line is a numerical solution of the one mode approximation and the dashed lines are from Eq. (37) for the lower solid-solid coexistence lines and Eq. (40) for the upper liquid-solid coexistence lines. The solid points are from numerical solutions for the minimum free energy functional given in Eq. (35).

$$C_{11}/3 = C_{12} = C_{44} = 3B^s(A_{\rm min})^2/16 \tag{41}$$

(this calculation can be done for arbitrary dependence of B^s on δN). As expected the elastic constants are directly proportional to the amplitude of the density fluctuations. This implies that the elastic constants decrease as the liquid-solid transition is approached from the solid phase. This result implies both a temperature and concentration dependence through the dependence of $A_{\rm min}$ on ΔB. In addition to this dependence (which might be considered as a thermodynamic dependence) the magnitude of the elastic constants can be altered by the constant B^s.

2. Calculation of alloy phase diagrams

To examine the validity of some of the approximations for the phase diagrams made in the preceding section, numerical simulations were conducted to determine the properties of the solid and liquid equilibrium states. The simulations were performed over a range of δN values, three values of ΔB_0 (0.07, 0.02, and −0.03) and two values of w (0.088 and −0.04). The specific values of the other constants that enter the model are given in the figure caption of Fig. 2.

In general the numerical results for the free energy, F, the lattice constant R and bulk modulus agreed quite well with the analytic one-mode predictions presented in the preceding section for all parameters. Comparisons of the analytic and numerical predictions for the phase diagram are shown in Figs. 2 and 3 for $w=0.088$ and −0.04, respectively. As seen in these figures the agreement is quite good except near the eutectic point shown in Fig. 3. In this case, the analytic cal-

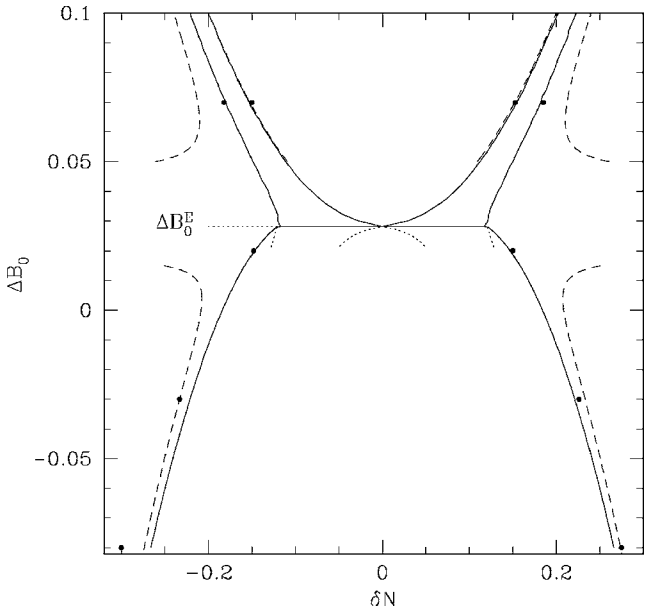

FIG. 3. Phase diagram of ΔB_0 vs δN for the same parameters as those used to generate Fig. 2, with the exception that $w=-0.04$. The dotted lines below the eutectic temperature, $\Delta B_0^E \approx 0.028$, correspond to metastable states.

culations [Eqs. (40) and (37)] for the coexistence lines breakdown at the eutectic point and higher order terms in δN are needed to accurately predict the phase diagram.

IV. DYNAMICS

To simulate microstructure formation in binary alloys, dynamical equations of motion for the fields δN and n need to be developed. The starting point is the full free energy in Eq. (15), written in terms of ρ_A and ρ_B, i.e., $\mathcal{F}(\rho_A, \rho_B)$. The dynamics of ρ_A and ρ_B is assumed to be dissipative and driven by free energy minimization, i.e.,

$$\frac{\partial \rho_A}{\partial t} = \nabla \cdot \left(M_A(\rho_A, \rho_B) \nabla \frac{\delta \mathcal{F}}{\delta \rho_A} \right) + \xi_A, \tag{42}$$

$$\frac{\partial \rho_B}{\partial t} = \nabla \cdot \left(M_B(\rho_A, \rho_B) \nabla \frac{\delta \mathcal{F}}{\delta \rho_B} \right) + \xi_B, \tag{43}$$

where M_A and M_B are the mobilities of each atomic species. In general these mobilities depend on the density of each species. The variables ξ_A and ξ_B are conserved Gaussian correlated noise fields that represent thermal fluctuation in the density of species A and B. They satisfy the fluctuation-dissipation theorm $\langle \xi_i^2 \rangle = -2k_B T M_i \nabla^2 \delta(\vec{r}-\vec{r}')\delta(t-t')$, where M_i is the mobility of A or B atoms. For simplicity the noise terms will be neglected in what follows.

The free energy $\mathcal{F}(\rho_A, \rho_B)$ can be equivalently defined in terms of n and δN. This allows the previous equations to be rewritten as

$$\frac{\partial n}{\partial t} = \vec{\nabla} \cdot \left\{ M_1 \vec{\nabla} \frac{\delta \mathcal{F}}{\delta n} \right\} + \vec{\nabla} \cdot \left\{ M_2 \vec{\nabla} \frac{\delta \mathcal{F}}{\delta(\delta N)} \right\}, \tag{44}$$

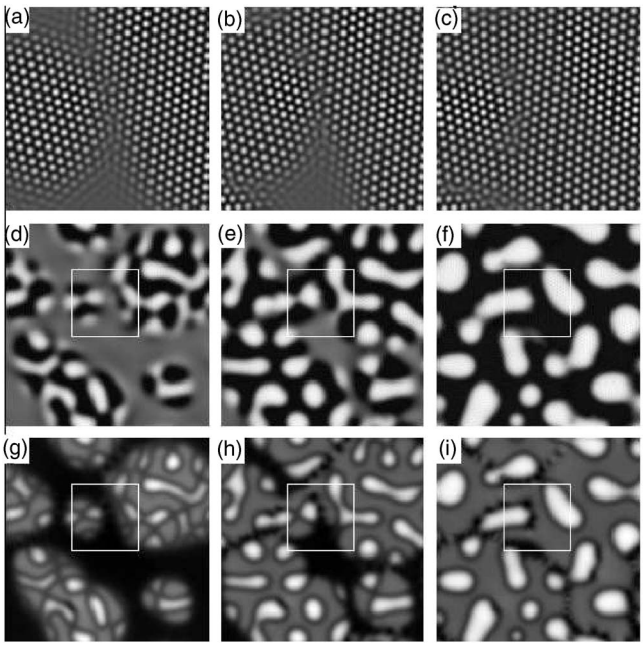

FIG. 4. The gray scales in the figure correspond to density (n), concentration (δN) and the local energy density in frames (a,b,c), (d,e,f), and (g,h,i), respectively. The area enclosed by white boxes is area shown in (a,b,c). The parameters in this simulation are the same as Fig. 3 except $L=1.20$ and $R_1/R_0=1/4$ ($R_0=1$), $\delta N=0$ and $\Delta B_0=0.02$. (a,d,g), (b,e,h), and (c,f,i) correspond to times $t=6600$, 16 200, 49 900, respectively.

$$\frac{\partial(\delta N)}{\partial t} = \vec{\nabla} \cdot \left\{ M_2 \vec{\nabla} \frac{\delta \mathcal{F}}{\delta n} \right\} + \vec{\nabla} \cdot \left\{ M_1 \vec{\nabla} \frac{\delta \mathcal{F}}{\delta(\delta N)} \right\}, \tag{45}$$

where $M_1 \equiv (M_A + M_B)/\bar{\rho}^2$ and $M_2 \equiv (M_B - M_A)/\bar{\rho}^2$. Equations (44) and (45) couple the dynamics of the fields δN and n through a symmetric mobility tensor. The dependence of the mobilities M_A and M_B will in general depend on local crystal density and the local relative concentration of species A and B.

For the case of substitutional diffusion between species A and B, $M_A \approx M_B \equiv M$. In this limit the dynamics of n and δN decouple. Moreover if it is further assumed that the mobility is a constant, Eqs. (44) and (45) become

$$\frac{\partial n}{\partial t} = M_e \nabla^2 \frac{\delta \mathcal{F}}{\delta n}, \tag{46}$$

$$\frac{\partial(\delta N)}{\partial t} = M_e \nabla^2 \frac{\delta \mathcal{F}}{\delta(\delta N)}, \tag{47}$$

where the effective mobility $M_e \equiv 2M/\bar{\rho}^2$. In the applications using Eqs. (46) and (47) in the following sections, the dynamics of n and δN are simulated with time rescaled by $t \rightarrow \bar{t} \equiv 2Mt/\bar{\rho}^2$.

To illustrate the dynamics described by Eqs. (46), (47), and (35), a simulation of heterogenous eutectic crystallization from a supercooled homogenous liquid was performed. The results of this simulation are shown in Fig. 4. This figure shows the density (n), the density difference (δN) and the

local energy density at three time steps in the solidification process. These figures show liquid-crystal interfaces, grain boundaries, phase segregation, dislocations and multiple crystal orientations all in a single numerical simulation of the simple binary alloy PFC model. In this simulation a simple Euler algorithm was used for the time derivative and the spherical Laplacian approximation was used. The grid size was $\Delta x=1.1$ and the time step was $\Delta t=0.05$. Unless otherwise specified all simulations to follow use the same algorithm, grid size, and time step.

V. APPLICATIONS

This section applies the simplified PFC model derived in Sec. III C, coupled to the dynamical equations of motion derived in Sec. IV, to the study of elastic and plastic effects in phase transformations. The first application demonstrates how the PFC alloy model can be used to simulate eutectic and dendritic microstructures. That is followed by a discussion of the effects of compressive and tensile stresses in epitaxial growth. Finally, simulations demonstrating the effects of dislocation motion in spinodal decomposition are presented.

A. Eutectic and dendritic solidification

One of the most important applications of the alloy PFC model is the study of solidification microstructures. These play a prominent role in numerous applications such as commercial casting. Traditional phase-field models of solidification are typically unable to self-consistently combine bulk elastic and plastic effects with phase transformation kinetics, multiple crystal orientations and surface tension anisotropy. While some of these effects have been included in previous approaches (e.g., surface tension anisotropy) they are usually introduced phenomenologically. In the PFC formalism, these features arise naturally from DFT.

To illustrate solidification microstructure formation using the PFC formalism, two simulations of Eqs. (46) and (47) were conducted of the growth of a single crystal from a supercooled melt in two dimensions. In the first simulation a small perturbation in the density field was introduced into a supercooled liquid using the parameters corresponding to the phase diagram in Fig. 3, except $L=1.20$ and $R_1/R_0=1/4$. The reduced temperature $\Delta B_0=0.0248$ and average concentration $\delta N=0.0$. To reduce computational time the size of the lattice was gradually increased as the seed increased in size. A snapshot of the seed is shown at $t=480\,000$ in Fig. 5(a). A similar simulation was conducted for the growth of a dendrite from a supercooled melt for reduced temperature $\Delta B_0=0.04$ and $\delta N=0.0904$, with other parameters corresponding to those in Fig. 2, except for $L=1.20$ and $R_1/R_0=1/4$. A sample dendritic structure is shown in Fig. 5(b) at $t=175\,000$. It should be noted that the dendrite in Fig. 5(b) is not sixfold symmetric about its main trunk because the simulation is influenced by the boundaries of the numerical simulation cell, which are fourfold symmetric. Dendrites nucleated and grown in the center of the simulation domain retain their sixfold symmetry. Finally, it should be stressed that the side-branching is only qualitatively correct in Fig. 5(b) as it was initiated by numerical grid noise. For a more quantitative simulation of nucleation and growth of side-branches, thermal fluctuations need to included in Eqs. (46) and (47).

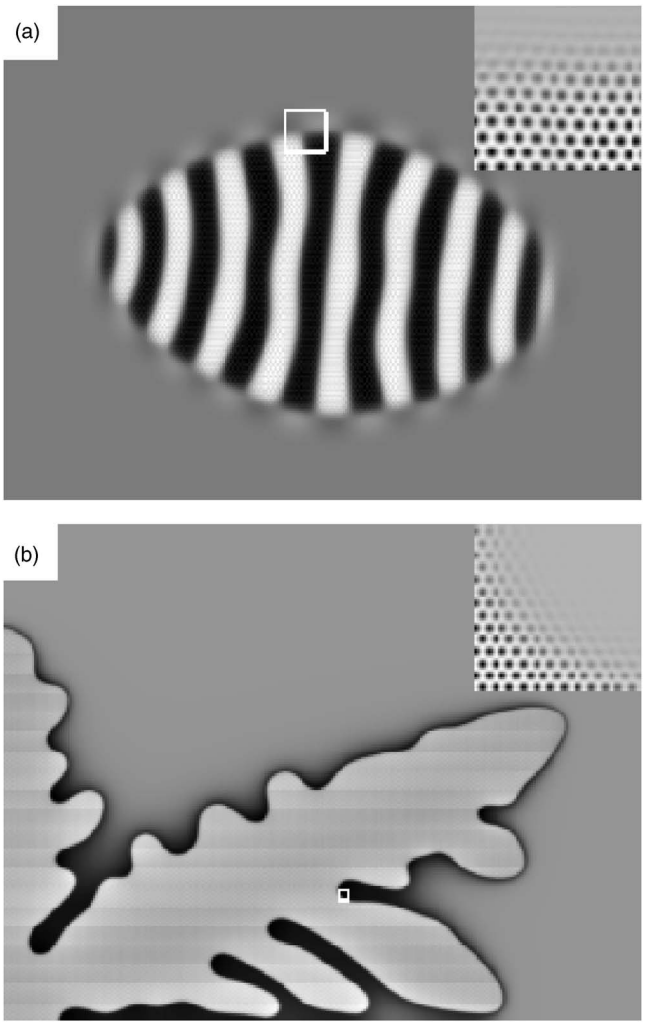

FIG. 5. The gray scale in the main portion of both figures show the concentration field δN. In the insets, the gray-scale shows the density field, n, for the small portion of the main figure that is indicated by the white boxes. (a) Eutectic crystal grown from a supercooled liquid at $\Delta B_0=0.0248$ and $\delta N=0.0$. The parameters that enter the model are the same as Fig. 3 except $L=1.20$ and $R_1/R_0=1/4$ ($R_0=1$). (b) Dendrite crystal grown from a supercooled liquid at $\Delta B_0=0.04$ and $\delta N=0.0904$. The parameters that enter the model are the same as Fig. 2 except $L=1.20$ and $R_1/R_0=1/4$. In (b) mirror boundary conditions were used.

Simulations such as these can play an important role in establishing various constitutive relations for use in higher-scale finite element modeling (FEM) of elastoplastic effects in alloys during deformation. In particular, traditional FEM approaches often employ empirical or experimental constitutive models to describe stress-strain response in elements that are intended to represent one (or more) grains. These constitutive relations are often limited in their usefulness as they do not self-consistently incorporate realistic information about microstructural properties that develop during solidification.

B. Epitaxial growth

Another potential application of the PFC model is in the technologically important process of thin film growth. The case of heteroepitaxy, the growth of a crystalline film exhibiting atomic coherency with a crystalline substrate of differing lattice constant, has been examined in previous PFC studies of pure systems.[33,34] These initial works focused on two of the primary phenomena influencing film quality: (i) morphological instability to buckling or roughening and (ii) dislocation nucleation at the film surface. A third important effect in alloy films, (iii) compositional instability (phase separation in the growing film), requires consideration of multiple atomic species and their interaction. The purpose of this section is to illustrate how the binary PFC model addresses such compositional effects in alloy heteroepitaxy, focusing on the spatial dynamics of phase separation over diffusive time scales.

To date, a number of models of single component film growth incorporating surface roughening, dislocation nucleation, or both have been proposed,[25,45–53] and models of binary film growth incorporating surface roughening and phase separation have been proposed as well.[54–57] However, no existing models of binary film growth known to the authors have captured all of the above important phenomena, and it would be reasonable to expect that new insights into the nature of film growth could be gained through the simultaneous investigation of all of these growth characteristics. A unified treatment of this sort is required for the following reasons. There is clearly a strong link between surface roughening and dislocation nucleation, originating from the fact that dislocations nucleate at surface cusps when the film becomes sufficiently rough. It is also known that phase separation in the film is significantly influenced by local stresses, which are inherently coupled to surface morphology and dislocation nucleation. The dynamics of the growth process must then be influenced by the cooperative evolution of all three of these phenomena. In the next paragraph numerical simulations will be presented to show that the binary PFC model produces all of the growth characteristics described above, and that each is influenced by misfit strain and atomic size and mobility differences between species.

Numerical simulations. The physical problem recreated in these simulations is that of growth of a symmetric (i.e., 50/50 mixture, or average density difference $\delta N_0=0$) binary alloy film from a liquid phase or from a saturated vapor phase above the bulk coherent spinodal temperature (ΔT_c). Growth at temperatures above the miscibility gap is typical of experimental conditions and should ensure that phase separation is driven by local stresses and is not due to spinodal decomposition. Initial conditions consisted of a binary, unstrained crystalline substrate, eight atoms in thickness, placed below a symmetric supercooled liquid of components A and B. In all the simulations presented, parameters are the same as in Fig. 2 except for $L=1.882$ and $\Delta B_0=0.008\,86$ unless specified in the figure caption. In what follows the misfit strain, ϵ, is defined as $(a_{\text{film}}-a_{\text{sub}})/a_{\text{sub}}$, where $a_{\text{film}} \approx a_A(1+\eta\delta N_0)$ if in the constant concentration approximation. For a symmetric mixture of A and B atoms (i.e., $\delta N_0=0$) $a_{\text{film}}=(a_A+a_B)/2$.

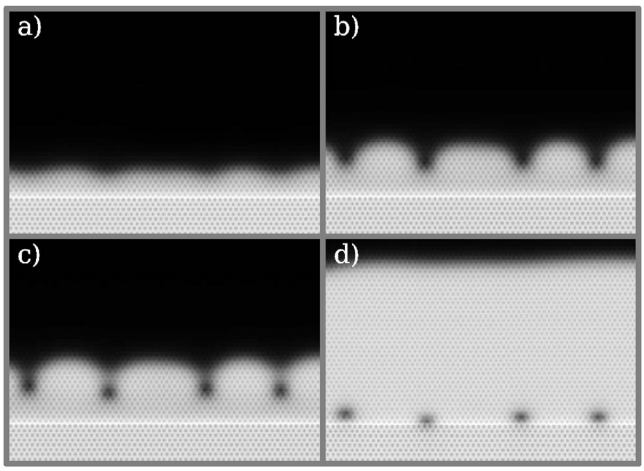

FIG. 6. Plots of the smoothed local free energy showing the progression of the buckling instability, dislocation nucleation and climb towards the film-substrate interface. From (a) to (d) times shown are $t=600$, 1050, 1200, and 2550. In this figure $\epsilon=0.04$, $\eta=-1/4$, and $M_A=M_B=1$.

Periodic boundary conditions were used in the lateral directions, while a mirror boundary condition was applied at the bottom of the substrate. A constant flux boundary condition was maintained along the top boundary, $120\Delta x$ above the film surface, to simulate a finite deposition rate. Misfit strain was applied to the system by setting $R=1$ in the substrate and $R=1+\epsilon+\eta\delta N$ in the film. This approach yields a film and substrate that are essentially identical in nature except for this shift in lattice parameter in the film. Complexities resulting from differing material properties between the film and substrate are therefore eliminated, isolating the effects of misfit strain, solute strain, and mobility differences on the film growth morphology. The substrate was permitted to strain elastically, but was prevented from decomposing compositionally except near the film-substrate interface.

A sample simulation is shown in Fig. 6 demonstrating that the well-documented buckling or Asaro-Tiller-Grinfeld[46,47] instability is naturally reproduced by the PFC model. This instability is ultimately suppressed as a cusplike surface morphology is approached, with increasingly greater stress developing in surface valleys. The buckling behavior ceases when the local stress in a given valley imparts on the film a greater energy than that possessed by an equivalent film with a dislocation. At this stage a dislocation is nucleated in the surface valley and the film surface begins to approach a planar morphology.

The nature of phase separation within the bulk film and at the film surface was found to vary with model parameters, but a number of generalizations applicable to all systems studied have been identified. For the case of equal species mobilities ($M_A=M_B$) we find that in the presence of misfit and solute strain, the component with greater misfit relative to the substrate preferentially segregates below surface peaks (see regions marked 1 and 2 in Fig. 7 and Fig. 8). Larger (smaller) atoms will be driven toward regions of tensile (compressive) stress which corresponds to peaks (valleys) in a compressively strained film and to valleys (peaks) in a film under tensile strain. This coupling creates a lateral phase

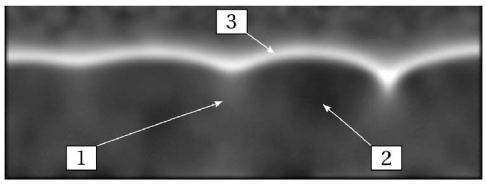

FIG. 7. Plot of the smoothed local concentration field showing lateral phase separation between the surface peaks and valleys. White, component A (large, fast); black, component B (small, slow). In this figure $\epsilon=-0.02$, $\eta=0.4$, $M_A=1$, $M_B=1/4$, and $t=3500$. See text for discussion of the numbered arrows.

separation on the length scale of the surface instability and has been predicted and verified for binary films[54–62] and analogous behavior has been predicted and verified in quantum dot structures.[63,64,67]

Second, again for the case of equal mobilities, the component with greater misfit relative to the substrate is driven toward the film surface (see Fig. 8). This behavior can also be explained in terms of stress relaxation and is somewhat analogous to impurity rejection in directional solidification. The greater misfit component can be viewed as an impurity that the growing film wishes to drive out toward the interface. Experimental evidence from SiGe on Si (Ref. 58) and InGaAs on InP (Refs. 59 and 60) verifies this behavior as an enrichment of the greater misfit component was detected at the film surface in both systems. Other models[54–57] have not led to this type of vertical phase separation possibly due to neglecting diffusion in the bulk films.

The third generalization that can be made is that, in the case of sufficiently unequal mobilities, the component with greater mobility accumulates at the film surface (see region marked 3 in (Fig. 7). It was found that when the two components have a significant mobility difference, typically greater than a 2:1 ratio, the effect of mobility is more important than the combined effects of misfit and solute strains in determining which component accumulates at the surface. Since Ge is believed to be the more mobile component in the SiGe system, we see that the findings of Walther *et al.*[58] for SiGe on Si provide experimental support for this claim. They find a significant enrichment of Ge at the film surface, a result that was likely due to a combination of this mobility driven effect as well as the misfit driven effect described in the second generalization. Experimental evidence also indicates that segregation of substrate constituents into the film may occur during film growth.[68,69] We have similarly found that a vertical phase separation is produced near the film-substrate interface and is complimented by a phase separation mirrored in direction near defects. The extent of this phase separation is controlled largely by the bulk mobilities of the two constituents, and to a lesser degree by η. The complimenting phase separation near climbing defects is a transient effect, any traces of which are dulled once the defect reaches the film-substrate interface.

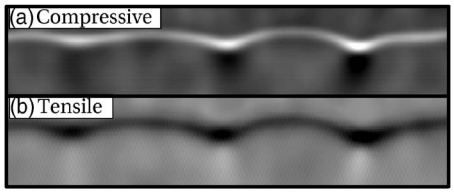

FIG. 8. Plot of the smoothed local concentration field showing the nature of the phase separation under opposite signs of ϵ. In (a) and (b) $\epsilon=0.04$ and -0.025, respectively, and in both figures $M_A=M_B=1$ and $\eta=0.25$.

C. Dislocation motion in spinodal decomposition

Spinodal decomposition is a nonequilibrium process in which a linearly unstable homogenous phase spontaneously decomposes into two daughter phases. An example of this process in the solid state occurs during a quench below the spinodal in Fig. 2 when $\delta N=0$. During this process domains of alternating concentration grow and coarsen to a scale of tens of nanometers. Spinodal decomposition is of interest as it is a common mechanism for strengthening alloys, due to the large number of interfaces that act to impede dislocation motion.

Solid state strengthening mechanisms, such as spinodal decomposition, rely critically on the interactions that exist between dislocations and phase boundaries. Cahn was first to calculate that the driving force for nucleation of an incoherent second phase precipitate is higher on a dislocation than in the bulk solid.[70] A similar result was obtained by Dolins for a coherent precipitate with isotropic elastic properties in the solid solution.[71] Hu *et al.* confirmed the results of Cahn and Dolins using a model that included elastic fields from compositional inhomogeneities and structural defects.[72]

Recent studies of spinodal decomposition have used phase-field models to examine the role of dislocations on alloy hardening.[73,74] These phase-field models couple the effects of static dislocations to the kinetics of phase separation. Léonard and Desai were the first to simulate the effect of static dislocations on phase boundaries, showing that the presence of dislocations strongly favors the phase separation of alloy components.[75]

Haataja *et al.* recently introduced mobile dislocations into a phase-field model that couples two burgers vectors fields to solute diffusion and elastic strain relaxation. It was shown that mobile dislocations altered the early and intermediate time coarsening regime in spinodal decomposition.[76,77] Specifically, it was found that coherent strains at phase boundaries decrease the initial coarsening rate, as they increase the stored elastic energy in the system. As dislocations migrate toward moving interfaces, they relax this excess strain energy, thus increasing the coarsening rate.[76] The growth regimes predicted by the model in Ref. 76 are in general agreement with several experimental studies of deformation on spinodal age hardening.[78–81]

Numerical simulations. Spinodal decomposition was simulated using Eqs. (46) and (47), for an alloy corresponding to the phase diagram in Fig. 2. Simulations began with a liquid phase of average dimensionless density difference $\delta N_0=0$, which first solidified into a polycrystalline solid (alpha) phase, which subsequently phase separated as the reduced temperature (ΔB_0) was lowered below the spinodal. Figure 9 shows the concentration and density fields for four

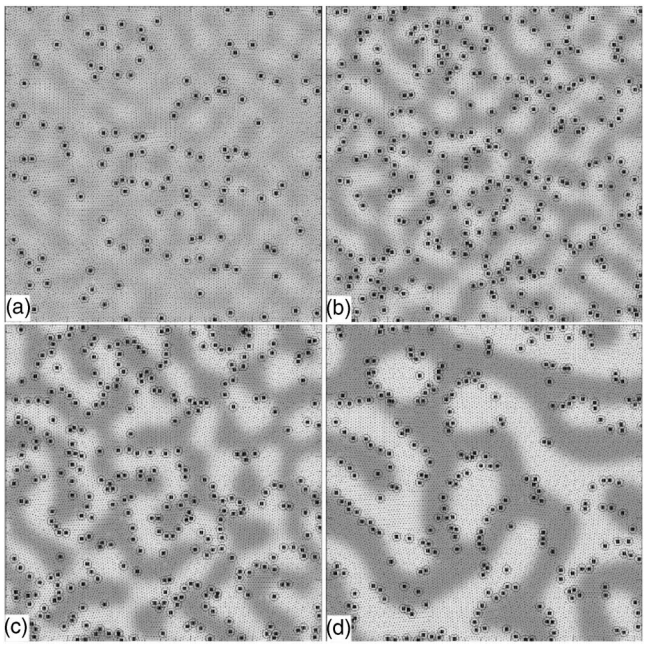

FIG. 9. Four time sequences in the evolution of the concentration field (gray scale), superimposed on the corresponding density field. Dislocations are labeled by a square on the dislocation core surrounded by a circle. The time sequence (a)–(d) corresponds to $t=12\,000$, 24 000, 60 000, and 288 000, respectively (in units of $\Delta t=0.004$). The system size is $1024\Delta x \times 1024\Delta x$, where $\Delta x=\pi/4$. The average density difference $\delta N_0=0$, while $L=2.65$, $R_1/R_0=1/4$ ($R_0=1$) and all other parameters are the same as Fig. 2.

time sequences during the spinodal decomposition process. The dots in the figures denote the locations of dislocation cores. Parameters for this simulation are given in the caption of Fig. 9. The spinodal coarsening rate corresponding to the data of Fig. 9 was found to exhibit an early and intermediate time regime that is slower that its traditional $t^{1/3}$ behavior, while at late times it asymptotically approaches $t^{1/3}$.

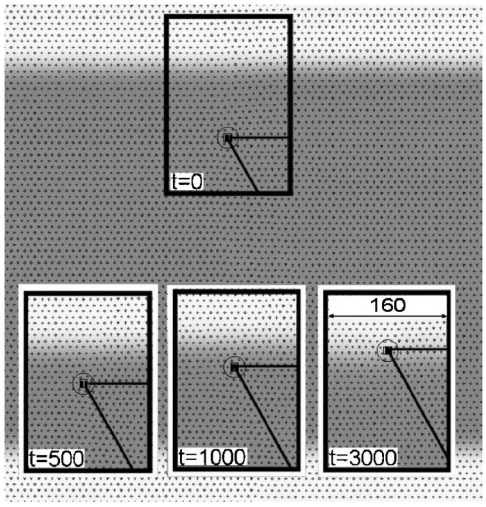

FIG. 10. A dislocation migrates toward a coherent phase boundary thus relaxing mismatch strain. An 800×800 (units of Δx) portion of the actual simulations domain is shown. The data shows four time frames in the motion of the dislocation. Parameters of the simulation are the same as in Fig. 9.

The simulations in Fig. 9 contain compositional domain boundaries *and* grain boundaries between grains of different orientations. As a result, the observed dislocation motion is affected by elastic strain energy due to phase separation and curvature driven grain boundary motion. To isolate the effect of phase separation on dislocations, Fig. 10 demonstrates dislocation motion near a coherent interface in the alloy. As in Ref. 76, coherent strain energy built up due to compositional differences in the two phases drives the dislocation toward the compositional boundary.

It is noteworthy that the alloy PFC introduced in this work does not incorporate "instantaneous" elastic relaxation. A proper treatment of rapid relaxation of strain fields requires the model to be extended in a manner analogous to Ref. 39. However, because of the asymptotically slow kinetics of spinodal decomposition and the small length scales between domain boundaries, it is expected that this will only influence the time scales over which dislocations interact with domain boundaries. As a result, the general trends depicted in (9) are expected to be correct.

VI. DISCUSSION AND CONCLUSIONS

In this paper a connection between the density functional theory of freezing and phase-field modeling was examined. More specifically it was shown that the phase-field crystal model introduced in earlier literature[33–35] and the regular solution commonly used in material science can be obtained from DFT in certain limits. These calculations relied on parametrizing the direct two-point correlation function that enters DFT by three quantities related to the elastic energy stored in the liquid and crystalline phases, as well as the lattice constant.

In addition, a simplified binary alloy model was developed that self-consistently incorporates many physical features inaccessible in other phase-field approaches. The simplified alloy PFC model was shown to be able to simultaneously model solidification, phase segregation, grain growth, elastic and plastic deformations in anisotropic systems with multiple crystal orientations on diffusive time scales.

It is expected that the alloy PFC formalism and its extensions can play an important role in linking material properties to microstructure development in a manner that *fundamentally* links the mesoscale to the atomic scale. As such this formalism, particularly when combined with adaptive mesh techniques in phase amplitude or reciprocal space, can lead the way to a truly multiscale methodology for predictive modeling of materials performance.

ACKNOWLEDGMENTS

One of the authors (K. R. E.) acknowledges support from the National Science Foundation under Grant No. DMR-0413062. Two of the authors (N. P. and M. G.) would like to thank the National Science and Engineering Research Council of Canada for financial support. One of the authors (M. G.) also acknowledges support from le Fonds Quebecois de

la recherche sur la nature et les technologies. One of the authors (J. B.) acknowledges support from the Richard H. Tomlinson Foundation.

APPENDIX: SIMPLE BINARY ALLOY MODEL

This appendix goes through the expansion required to arrive at the simplified alloy model presented in Sec. III B. For this calculation the free energy functional in Eq. (16) is expanded in the variables n and δN, as defined in Eq. (34), up to order four (noting that terms of order n or δN can be dropped since they integrate to zero in the free energy functional as they are all defined around their average values). In addition it will be assumed that δN varies on length scales much larger than n. This is reasonable on long-time (diffusion) times scales, where solute and host atoms intermix on length scales many times larger than the atomic radius. This assumption allows terms of order $n\delta N$ to be eliminated from the free energy. The result of these expansions and approximations is that the free energy functional can be written as

$$\frac{\mathcal{F}}{\bar{\rho}k_BT} = \int d\vec{r}\Bigg[f_0 + B^\ell\frac{n^2}{2} - \frac{n^3}{6} + \frac{n^4}{12} + nF\nabla^2 n + \frac{\delta N}{2}\left(1 - \frac{C^{AA} + C^{BB} - 2C^{AB}}{4}\right)\delta N + \frac{\delta N^4}{12} + \frac{\beta}{2\bar{\rho}}(1-n^3)\delta N + nG\nabla^4 n + \frac{dC}{4\bar{\rho}}[(\bar{\rho}-\rho_\ell)^2 - \rho_\ell^2 n^3]\delta N\Bigg], \tag{A1}$$

where

$$f_0 = \ln\left(\frac{\bar{\rho}}{2\rho_\ell}\right) - (1-\rho_\ell/\bar{\rho}) - \bar{\rho}\hat{C}_0^{AB}/4 - \frac{1}{8}(\bar{\rho} + 2\rho_\ell^2/\bar{\rho} - 4\rho_\ell)\times(\hat{C}_0^{AA} + \hat{C}_0^{BB}),$$

$$B^\ell = 1 - \bar{\rho}\hat{\bar{C}}_0 + \bar{\rho}^{-1}(\beta + \rho_\ell^2 d\hat{C}_0/2)\delta N + \delta N^2,$$

$$F = -\bar{\rho}\hat{\bar{C}}_2 + \rho_\ell^2 d\hat{C}_2\delta N/2\bar{\rho},$$

$$G = -\bar{\rho}\hat{\bar{C}}_4 + \rho_\ell^2 d\hat{C}_4\delta N/2\bar{\rho},$$

$$dC = C^{AA} - C^{BB}, \tag{A2}$$

while $\hat{\bar{C}}_n \equiv (\hat{C}_n^{AA} + \hat{C}_n^{BB} + 2\hat{C}_n^{AB})/4$ and $d\hat{C}_n \equiv \hat{C}_n^{AA} - \hat{C}_n^{BB}$.

The preceding equation can finally be cast into a form similar to that presented in Sec. III C of the text,

$$\frac{\mathcal{F}}{\bar{\rho}k_BT} = \int d\vec{r}\left(f_0 + \frac{n}{2}[B^\ell + B^s(2R^2\nabla^2 + R^4\nabla^4)]n - \frac{n^3}{6} + \frac{n^4}{12} + \frac{w}{2}\delta N^2 + \frac{\delta N^4}{12} + \frac{L^2}{2}|\nabla\delta N|^2 + \gamma\delta N + \frac{H^4}{2}\delta N\nabla^4\delta N\right), \tag{A3}$$

where $B^s = F^2/(2G)$, $R = \sqrt{2G/F}$, $w = (1 - \Delta\hat{C}_0/2)$, $L^2 = \Delta\hat{C}_2/2$, $H^2 = -\Delta\hat{C}_4/2$, and $2\bar{\rho}\gamma = \beta(1-n^3) + dC[(\bar{\rho}-\rho_\ell)^2 - \rho_\ell^2 n^3]/2$ [$\Delta\hat{C}_n$ as in Eq. (20)].

The dependence of the coefficients in B^l, B^ℓ, and R on the density difference can be explicitly obtained by expanding them in δN as well. This gives,

$$B^\ell = B_0^\ell + B_1^\ell\delta N + B_2^\ell\delta N^2,$$

$$B^s = B_0^s + B_1^s\delta N + B_2^s\delta N^2 + \cdots,$$

$$R = R_0 + R_1\delta N + R_2\delta N^2 + \cdots, \tag{A4}$$

where $B_0^\ell = 1 - \bar{\rho}\hat{\bar{C}}_0$, $\bar{\rho}B_1^\ell = \beta + \rho_\ell^2 d\hat{C}_0/2$, $B_2^\ell = 1$, $B_0^s = -\bar{\rho}(\hat{\bar{C}}_2)^2/\hat{\bar{C}}_4$, $B_1^s = -\hat{\bar{C}}_2\rho_\ell^2(\hat{\bar{C}}_2 d\hat{C}_4 - 2\hat{\bar{C}}_4 d\hat{C}_2)/4\bar{\rho}\hat{\bar{C}}_4^2$, $B_2^s = -\rho_\ell^2(\hat{\bar{C}}_2 d\hat{C}_4 - \hat{\bar{C}}_4 d\hat{C}_2)^2/8\bar{\rho}^3\hat{\bar{C}}_4^3$, $R_0 = \sqrt{2\hat{\bar{C}}_4/\hat{\bar{C}}_2}$, $R_1/R_0 = -\rho_\ell^2(d\hat{C}_4/\hat{\bar{C}}_4 - d\hat{C}_2/\hat{\bar{C}}_2)/4\bar{\rho}^2$, and $R_2/R_0 = -\rho_\ell^4(\hat{\bar{C}}_2 d\hat{C}_4 - \hat{\bar{C}}_4 d\hat{C}_2)(\hat{\bar{C}}_2 d\hat{C}_4 + 3\hat{\bar{C}}_4 d\hat{C}_2)/32\bar{\rho}^4\hat{\bar{C}}_4^2\hat{\bar{C}}_2^2$.

[1] J. W. Cahn and J. E. Hilliard, J. Chem. Phys. **28**, 258 (1958); H. E. Cook, Acta Metall. **18**, 297 (1970).
[2] S. M. Allen and J. W. Cahn, Acta Metall. **23**, 1017 (1975); **24**, 425 (1976); **27**, 1085 (1979).
[3] L. Leibler, Macromolecules **13**, 1602 (1980); Y. Oono and Y. Shiwa, Mod. Phys. Lett. B **1**, 49 (1987).
[4] J. B. Collins and H. Levine, Phys. Rev. B **31**, 6119 (1985).
[5] J. S. Langer, *Directions in Condensed Matter* (World Scientific, Singapore, 1986), p. 164.
[6] B. Grossmann, K. R. Elder, M. Grant, and J. M. Kosterlitz, Phys. Rev. Lett. **71**, 3323 (1993).
[7] K. R. Elder, F. Drolet, J. M. Kosterlitz, and M. Grant, Phys. Rev. Lett. **72**, 677 (1994); F. Drolet, K. R. Elder, M. Grant, and J. M. Kosterlitz, Phys. Rev. E **61**, 6705 (2000).
[8] J. A. Warren and W. J. Boettinger, Acta Metall. Mater. **43**, 689 (1995).
[9] G. Caginalp and X. Chen, in *On the Evolution of Boundaries*, edited by M. E. Gurtin and G. B. McFadden, IMA Volumes in Mathematics and its Applications, 43 (Springer-Verlag, New York, 1992), p. 1.
[10] R. Kobayashi, Physica D **63**, 410 (1993).
[11] S.-L. Wang, R. F. Sekerka, A. A. Wheeler, B. T. Murray, S. R. Coriell, R. J. Braun, and G. B. McFadden, Physica D **69**, 189 (1993).
[12] A. Karma and W.-J. Rappel, Phys. Rev. E **53**, R3017 (1996).
[13] A. Karma, Phys. Rev. Lett. **87**, 115701 (2001).
[14] K. R. Elder, M. Grant, N. Provatas, and J. M. Kosterlitz, Phys. Rev. E **64**, 021604 (2001).
[15] N. Provatas, M. Greenwood, B. Athreya, N. Goldenfeld, and J. Dantzig, Int. J. Mod. Phys. B **19**, 4525 (2005).

[16] N. Provatas, N. Goldenfeld, and J. Dantzig, Phys. Rev. Lett. **80**, 3308 (1998).
[17] N. Provatas, J. Dantzig, and N. Goldenfeld, J. Comput. Phys. **148**, 265 (1999).
[18] N. Provatas, N. Goldenfeld, J. Dantzig, J. C. LaCombe, A. Lupulescu, M. B. Koss, M. E. Glicksman, and R. Almgren, Phys. Rev. Lett. **82**, 4496 (1999).
[19] N. Provatas, Q. Wang, M. Haataja, and M. Grant, Phys. Rev. Lett. **91**, 155502 (2003).
[20] C. W. Lan, Y. C. Chang, and C. J. Shih, Acta Mater. **51**, 1857 (2003).
[21] M. Greenwood, M. Haataja, and N. Provatas, Phys. Rev. Lett. **93**, 246101 (2004).
[22] C. W. Lan and C. J. Shih, J. Cryst. Growth **2**, 472 (2004).
[23] Y. U. Wang, Y. M. Jin, A. M. Cuitino, and A. G. Khachaturyan, Appl. Phys. Lett. **78**, 2324 (2001); Philos. Mag. Lett. **81**, 385 (2001); Acta Mater. **49**, 1847 (2001).
[24] Y. M. Jin and A. G. Khachaturyan, Philos. Mag. Lett. **81**, 607 (2001).
[25] M. Haataja, J. Müller, A. D. Rutenberg, and M. Grant, Phys. Rev. B **65**, 165414 (2002).
[26] Y. Wang and A. G. Khachaturyan, Acta Metall. Mater. **43**, 1837 (1995); Acta Mater. **45**, 759 (1997).
[27] L. Q. Chen and A. G. Khachaturyan, Scr. Metall. Mater. **25**, 61 (1991).
[28] L.-Q. Chen and W. Yang, Phys. Rev. B **50**, 15752 (1994).
[29] B. Morin, K. R. Elder, M. Sutton, and M. Grant, Phys. Rev. Lett. **75**, 2156 (1995).
[30] J. A. Warren, W. C. Carter, and R. Kobayashi, Physica A **261**, 159 (1998); J. A. Warren, R. Kobayashi, and W. C. Carter, J. Cryst. Growth **211**, 18 (2000); R. Kobayashi, J. A. Warren, and W. C. Carter, Physica D **140**, 141 (2000).
[31] J. A. Warren, R. Kobayashi, A. E. Lobkovsky, and W. C. Carter, Acta Mater. **51**, 6035 (2003).
[32] L. Granasy, T. Pusztai, and J. A. Warren, J. Phys.: Condens. Matter **16**, R1205 (2004); L. Granasy, T. Pusztai, T. Borzsonyi, J. A. Warren, B. Kvamme, and P. F. James, Phys. Chem. Glasses **45**, 107 (2004).
[33] K. R. Elder, M. Katakowski, M. Haataja, and M. Grant, Phys. Rev. Lett. **88**, 245701 (2002).
[34] K. R. Elder and M. Grant, Phys. Rev. E **70**, 051605 (2004).
[35] J. Berry, M. Grant, and K. R. Elder, Phys. Rev. E **73**, 031609 (2006).
[36] Y. M. Jin and A. G. Khachaturyan, J. Appl. Phys. **100**, 013519 (2006).
[37] N. Goldenfeld, B. P. Athreya, and J. A. Dantzig, Phys. Rev. E **72**, 020601(R) (2005).
[38] N. Goldenfeld, B. P. Athreya, and J. A. Dantzig, J. Stat. Phys. **125**, 1015 (2006).
[39] P. Stefanovic, M. Haataja, and N. Provatas, Phys. Rev. Lett. **96**, 225504 (2006).
[40] K.-A. Wu, Ph.D. thesis, Northeastern University, 2006.
[41] K.-A. Wu, A. Karma, J. J. Hoyt, and M. Asta, Phys. Rev. B **73**, 094101 (2006).
[42] T. V. Ramakrishnan and M. Yussouff, Phys. Rev. B **19**, 2775 (1979).
[43] Y. Singh, Phys. Rep. **207**, 351 (1991).
[44] R. Evans, Adv. Phys. **28**, 143 (1979).
[45] J. W. Matthews and A. E. Blakeslee, J. Cryst. Growth **27**, 118 (1974); J. W. Matthews, J. Vac. Sci. Technol. **12**, 126 (1975).
[46] R. J. Asaro and W. A. Tiller, Metall. Trans. **3**, 1789 (1972).
[47] M. Grinfeld, J. Nonlinear Sci. **3**, 35 (1993); Dokl. Akad. Nauk SSSR **290**, 1358 (1986); [Sov. Phys. Dokl. **31**, 831 (1986)].
[48] R. People and J. C. Bean, Appl. Phys. Lett. **47**, 322 (1985).
[49] J. Müller and M. Grant, Phys. Rev. Lett. **82**, 1736 (1999).
[50] W. H. Yang and D. J. Srolovitz, Phys. Rev. Lett. **71**, 1593 (1993).
[51] K. Kassner, C. Misbah, J. Müller, J. Kappey, and P. Kohlert, Phys. Rev. E **63**, 036117 (2001).
[52] J. Tersoff and F. K. LeGoues, Phys. Rev. Lett. **72**, 3570 (1994).
[53] H. Gao and W. D. Nix, Annu. Rev. Mater. Sci. **29**, 173 (1999).
[54] B. J. Spencer, P. W. Voorhees, and J. Tersoff, Phys. Rev. Lett. **84**, 2449 2000; Phys. Rev. B **64**, 235318 (2001).
[55] J. E. Guyer and P. W. Voorhees, Phys. Rev. B **54**, 11710 (1996); Phys. Rev. Lett. **74**, 4031 (1995); J. Cryst. Growth **187**, 150 (1998).
[56] Z. F. Huang and R. C. Desai, Phys. Rev. B **65**, 195421 (2002); **65**, 205419 (2002).
[57] F. Leonard and R. C. Desai, Phys. Rev. B **56**, 4955 (1997); **57**, 4805 (1998).
[58] T. Walther, C. J. Humphries, and A. G. Cullis, Appl. Phys. Lett. **71**, 809 (1997).
[59] T. Okada, G. C. Weatherly, and D. W. McComb, J. Appl. Phys. **81**, 2185 (1997).
[60] F. Peiro, A. Cornet, J. R. Morante, A. Georgakilas, C. Wood, and A. Christou, Appl. Phys. Lett. **66**, 2391 (1995).
[61] J. Mirecki Millunchick, R. D. Twesten, D. M. Follstaedt, S. R. Lee, E. D. Jones, Y. Zhang, S. P. Ahrenkiel, and A. Mascarenhas, Appl. Phys. Lett. **70**, 1402 (1997).
[62] D. D. Perovic, B. Bahierathan, H. Lafontaine, D. C. Houghton, and D. W. McComb, Physica A **239**, 11 (1997).
[63] N. Liu, J. Tersoff, O. Baklenov, A. L. Holmes, Jr., and C. K. Shih, Phys. Rev. Lett. **84**, 334 (2000).
[64] J. Tersoff, Phys. Rev. Lett. **81**, 3183 (1998).
[65] M. Asta and J. J. Hoyt, Acta Mater. **48**, 1089 (2000).
[66] J. Mainville, Y. S. Yang, K. R. Elder, M. Sutton, K. F. Ludwig, Jr., and G. B. Stephenson, Phys. Rev. Lett. **78**, 2787 (1997).
[67] F. Ratto, F. Rosei, A. Locatelli, S. Cherifi, S. Fontana, S. Heun, P. D. Szkutnik, A. Sgarlate, M. De Crescenzi, and N. Motta, Appl. Phys. Lett. **84**, 4526 (2004).
[68] B. A. Joyce, J. L. Sudijono, J. G. Belk, H. Yamaguchi, X. M. Zhang, H. T. Dobbs, A. Zangwill, D. D. Vvedensky, and T. S. Jones, Jpn. J. Appl. Phys., Part 1 **36**, 4111 (1997).
[69] M. Krishnamurthy, A. Lorke, M. Wassermeier, D. R. M. Williams, and P. M. Petroff, J. Vac. Sci. Technol. B **11**, 1384 (1993).
[70] J. W. Cahn, Acta Metall. **5**, 169 (1957).
[71] C. C. Dolins, Acta Metall. **18**, 1209 (1970).
[72] S. Y. Hu and L. Q. Chen, Acta Mater. **49**, 463 (2001).
[73] D. Rodney, Y. Le Bouar, and A. Finel, Acta Mater. **51**, 17 (2003).
[74] J. W. Cahn, Acta Metall. **11**, 1275 (1963).
[75] F. Léonard and R. C Desai, Phys. Rev. B **58**, 8277 (1998).
[76] Mikko Haataja, Jennifer Mahon, Nikolas Provatas, and Francois Léonard, Appl. Phys. Lett. **87**, 251901 (2005).
[77] Mikko Haataja and Francois Léonard, Phys. Rev. B **69**, 081201(R) (2004).
[78] R. R. Bhat and P. P. Rao, Z. Metallkd. **75**, 237 (1994).
[79] F. T. Helmi and L. Zsoldos, Scr. Metall. **11**, 899 (1977).
[80] S. Spooner and B. G. Lefevre, Metall. Trans. A **11A**, 1085 (1975).
[81] J. T. Plewes, Metall. Trans. A **6A**, 537 (1975).